ACI MATERIALS JOURNAL TECHNICAL PAPER

Title no. 109-M05

Fracture Surface-Based Toughness Modeling of Cement-Based Materials

by Anne B. (Abell) Nichols and David A. Lange

One of the major principles of fracture mechanics of brittle materials is that the energy consumed in extending a crack through the material is related to the newly created surfaces, or surface energy. For ductile materials such as steel, fracture is dominated by plastic mechanisms, and surface energy is a small component. For quasi-brittle materials such as concrete, "pseudo-ductile" behavior results from the heterogeneous microstructure that causes cracks to deflect through a complex assembly of brittle phases and porosity. This study explores the hypothesis that the rough surfaces created by the fracture process can be used to characterize the fracture behavior of quasi-brittle materials. Several methods are used to measure the geometry of the fracture surface, along with subsurface cracking. Novel specimen preparation methods and measurement techniques were employed to assess fractured specimens. Mechanical tests were performed to measure fracture toughness. A model is proposed to link fracture surface parameters to fracture toughness.

Keywords: cement; fracture surface; image analysis; modeling; mortar; toughness.

INTRODUCTION

The fracture behavior of concrete has challenged researchers for several decades. Fracture mechanics has been pursued to understand empirical design formulas[1,2] and provide a basis for uniform safety margins, service performance, and failure analysis. As an engineering tool, it has been applied to concrete since 1959.[3] The theory of linear elastic fracture mechanics (LEFM) has been in use since 1920, but is not fully satisfactory for concrete materials. Concrete exhibits a nonlinear stress-strain behavior near the maximum load and strain-softening behavior thereafter, and researchers have shown that cracking in concrete is characterized by a relatively large process zone at the crack tip. Thus, investigation with LEFM has not been successful for understanding the fracture process of concrete.[4]

The fracture process includes creation of microcracks, localization of those cracks, and propagation of a macrocrack that separates the material. The energy expended in the fracture process is indicated by the toughness of the material. To better characterize the relationship of the microstructure of cement-based materials to the fracture process, researchers have investigated the microstructure to predict and explain the behavior by direct and indirect observation and through modeling of this complex system. It is through understanding this relationship that these materials can be changed and improved.

To model the fracture energy, it is necessary to quantify the toughening mechanisms on the crack path. The fracture surfaces are tortuous and the crack propagates through multiple phases of the microstructure, including the bulk cement paste, interfacial zone, air voids, and aggregate. Cracking occurs within the material adjacent to the fracture surface, and aggregate may interlock as the surfaces separate. Crack branching and interlock are mechanisms requiring additional energy during fracture and can be quantified by the overall amount of nonsurface cracks.

To quantify the geometry and phases of the fracture surface and crack branching—fracture surface characterization—Wood's metal intrusion and image analysis were used in this investigation, while the fracture energy from the load-displacement relationship was measured by mechanical testing. A micromechanical model was developed to describe the influence of the elastic modulus of the surface material components, the deflection by the aggregate inclusions, and the amount of subsurface cracking on the measured fracture toughness.

This research investigates the fracture behavior of several silica aggregate mortar systems and one concrete system. The corresponding geometry of the fracture surface features and cracks obtained with laser-scanning confocal microscopy and scanning electron microscopy (SEM) is used by a model that determines the increase in toughness from a theoretical flat crack fracture to toughness measured by mechanical testing. The indication of the research is that, even with different surface measurement techniques and relative scales from mortar to concrete, there is a convergence toward a single material toughness value representing the planar fracture for the cement composite devoid of toughening mechanisms.

RESEARCH SIGNIFICANCE

The fracture and toughness characteristics of cement-based materials are fundamental to the durability and performance of the infrastructure and structures. Understanding the mechanisms at the microstructural level can inform the design and effective use of these materials. The influence of the mechanisms involved in the fracture process is not directly observable or easily isolated, but a relationship exists between the constituents on and near the fracture path and the mechanisms. Modeling of the process, while relying on post-fracture microstructural evidence, can be used to characterize the relative or combined contribution to the energy involved in fracture, as indicated by toughness. This investigation models the micromechanical fracture behavior for well-defined mortar compositions and a comparable concrete composition using measurements of the crack deflection and constituents from the fracture surface and subsurface cracking to relate the measured fracture toughness to a theoretical flat crack toughness for the cement paste matrix material.

ACI Materials Journal, V. 109, No. 1, January-February 2012.

MS No. M-2009-336.R3 received January 28, 2011, and reviewed under Institute publication policies. Pertinent discussion including author's closure, if any, will be published in the November-December 2012 *ACI Materials Journal* if the discussion is received by August 1, 2012.

ACI member **Anne B. (Abell) Nichols** *is an Assistant Professor of architecture at Texas A&M University, College Station, TX. She received her PhD in civil engineering from the University of Illinois at Urbana-Champaign, Urbana, IL. Her research interests include microstructure of masonry and cement materials, fracture mechanics, and modeling.*

David A. Lange, *FACI, is a Professor of civil engineering at the University of Illinois at Urbana-Champaign. He received his PhD from Northwestern University, Evanston, IL. He is Chair of the ACI Technical Activities Committee, and a member of ACI Committees 236, Material Science of Concrete; 237, Self-Consolidating Concrete; 544, Fiber-Reinforced Concrete; S802, Teaching Methods and Educational Materials; and S803, Faculty Network Coordinating Committee. His research interests include early-age properties of concrete, microstructure of porous materials, and shrinkage and creep of concrete.*

EXPERIMENTAL PROCEDURE

To measure energy of fracture and obtain cracked and separated surfaces, mortar flexure specimens and concrete flexure specimens were mechanically tested. The composition of the materials with respect to aggregate type, aggregate volume, and entrained air was controlled to examine the influence of the surface inclusions and voids. Fracture surfaces were obtained for the mortars and concrete. Crack profiles were obtained for the mortars. The topography of the mortar and concrete fracture surfaces and profiles of the mortar cracks was obtained by microscopy and was quantified using image analysis techniques.

Materials

Five mixtures were cast for the mortar specimens and one mixture was cast for the concrete specimens. All mixtures used ordinary portland cement (OPC) with a water-cement ratio (*w*/*c*) of 0.5. A fluorescent dye (glycol ether-based) was added at 5% by weight of water to characterize paste at the surface of the mortars. Previous testing showed that the addition of the dye did not significantly alter the fracture behavior and material properties.[5] 20/30 ASTM C778 silica sand was used for the mortars (0.85 to 0.60 mm [0.03 to 0.02 in.]) at cement-to-sand ratios of 1:1 and 1:2. For two additional mortars, an air-entraining agent was added at 0.3% weight of cement to examine the shielding effect of voids on the crack. The aggregate for a control set (E) was smooth-surfaced alumina ceramic balls (0.79 to 1.18 mm [0.03 to 0.05 in.]) for preferential cracking at the interface. The content of alumina balls in the mortar was based on the equivalent volume of silica sand for a 1:1 ratio of cement to sand by weight. The bulk densities of the silica sand and ceramic balls were measured as 1.755 and 2.104 g/cm^3 (110 and 131 lb/ft^3), respectively. The aggregate for the concrete was crushed limestone with a maximum size of 19 mm (3/4 in.) and washed gravelly sand. The mortar mixture specifications and fresh air content as measured by ASTM C185 and adjusted for silica sand content are presented in Table 1. The concrete mixture specification as determined by the ACI 211.1 mixture design method is presented in Table 2, while the properties for the aggregates of the concrete mixture are listed in Table 3.

Specimens

All mortar specimens were cast as 178 x 38 x 24 mm (7 x 1.5 x 1 in.) beams with a cast notch at midspan of 12.7 mm (0.5 in.). The mold piece for the notch was 3 mm (0.12 in.) wide with a 90-degree point and fit into a socket in the mold base. The ceramic aggregate mortar (Set E) was cast within the central 15 mm (0.6 in.) of the specimen span with the remainder of the beam cast with plain, undyed paste. All mortar beams were cured in the horizontal position.

The concrete specimens were cast as 711 x 152 x 102 mm (28 x 6 x 4 in.) beams with a cast notch at midspan of 51 mm (2 in.). The mold piece for the notch was 12.7 mm (0.5 in.) wide with a 90-degree point and fit into a socket in the mold base. The concrete beams were geometrically proportional to the mortar beams by a factor of 4.

All specimens were cured in laboratory conditions for 1 day and then moist-cured for a total of 14 days prior to mechanical testing of the notched beams in three-point bending following the recommendations of the RILEM test method for determination of fracture parameters.[6]

Fracture toughness testing

The two-parameter fracture model (TPFM)[7] method determines the critical stress intensity factor K_{Ic}^S and the critical crack tip opening displacement $CTOD_c$ of mortar and plain concrete using three-point bend tests on notched beams.[6] The test is conducted on a closed-loop testing machine using the crack mouth opening displacement (CMOD) as the feedback signal. A constant rate of CMOD is applied until the load passes the peak load and is approximately 95% of the peak load, at which point the applied load is reduced. After unloading, the loading is applied again at the same initial rate. The initial compliance determined from the load-CMOD curve, the unloading compliance at 95% of peak load, and beam geometry parameters are used to calculate the modulus of elasticity, critical effective crack length, critical stress intensity factor K_{Ic}, and critical crack tip opening displacement $CTOD_c$.[6]

Only one cycle of the loading and unloading is required for the test, not necessarily resulting in separation. To obtain the fracture surfaces for this investigation, four beams from each mortar and concrete set were loaded to separation. Two beams of each mortar were not loaded to separation so that the branching of the main crack could be characterized. One beam was loaded to 75% of peak load on the second loading

Table 1—Mortar mixture proportions

Set	Number of specimens	*w*/*c*	Cement:sand ratio by weight	Fluorescent dye (by weight water), %	Air entrainment (by weight cement), %	Fresh mortar air content, %
A	6	0.5	1:1	5	—	0.82
B	6	0.5	1:1	5	0.3	3.57
C	6	0.5	1:2	5	—	1.85
D	6	0.5	1:2	5	0.3	7.70
E	6	0.5	1:1*	5	—	0.82

*Based on equivalent volume of ceramic alumina balls.

cycle, whereas the second was loaded to 85% of peak load on the second loading cycle. A mortar wedge was inserted in the notch opening to prevent any inadvertent closure. The load-CMOD diagrams for the mortar and concrete beam tests are presented in Fig. 1.

The values of the critical stress intensity factor determined from the two-parameter fracture method (Table 4) were lowest for the air-entrained mortars (Sets B and D) and the alumina ball mortar (Set E), although all these values are greater than 235 × 10^3 N/m$^{1.5}$ (0.21 kips/in.$^{1.5}$) determined in a previous study for mortar fracture specimens having the same geometry and notch length with OPC and a *w/c* of 0.45 tested at 28 days using the same test method.[8] Radjy and Hansen[9] presented the analytical (LEFM) value for K_{Ic} as 170 × 10^3 N/m$^{1.5}$ (0.15 kips/in.$^{1.5}$) for Type I OPC pastes with a *w/c* of 0.5 determined from slow bend tests by Moavenzadeh and Kuguel[10] on specimens with a size of 25 x 25 x 300 mm (1 x 1 x 12 in.) having a 10 mm (0.4 in.) notch. The analytical value of the critical stress intensity factor determined for cement-based materials is consistently lower than the value determined by the two-parameter fracture method.[11] The increase in the critical stress intensity factor measured for mortar set C, which has a greater aggregate volume than mortar set A (without air entrainment), is not repeated between mortar sets B and D having matching cement-to-sand ratios as sets A and C, respectively, but with entrained air. The value of the critical

Table 2—Concrete mixture proportions

Number of specimens	*w/c*	Water, kg/m^3 (lb/yd^3)	Cement, kg/m^3 (lb/yd^3)	Coarse aggregate,* kg/m^3 (lb/yd^3)	Fine aggregate,* kg/m^3 (lb/yd^3)
4	0.5	178 (300)	356 (600)	1197 (2018)	681 (1148)

*Surface-saturated dry.

Table 3—Concrete aggregate properties

Coarse aggregate	Fine aggregate
TM = 0.8%	TM = 2.08%
AC = 1.4%	AC = 1.8%
γ_{SSD} = 2.68	γ_{SSD} = 2.6
Unit weight SSD = 1624 kg/m^3 (101.40 lb/ft^3)	FM = 2.63

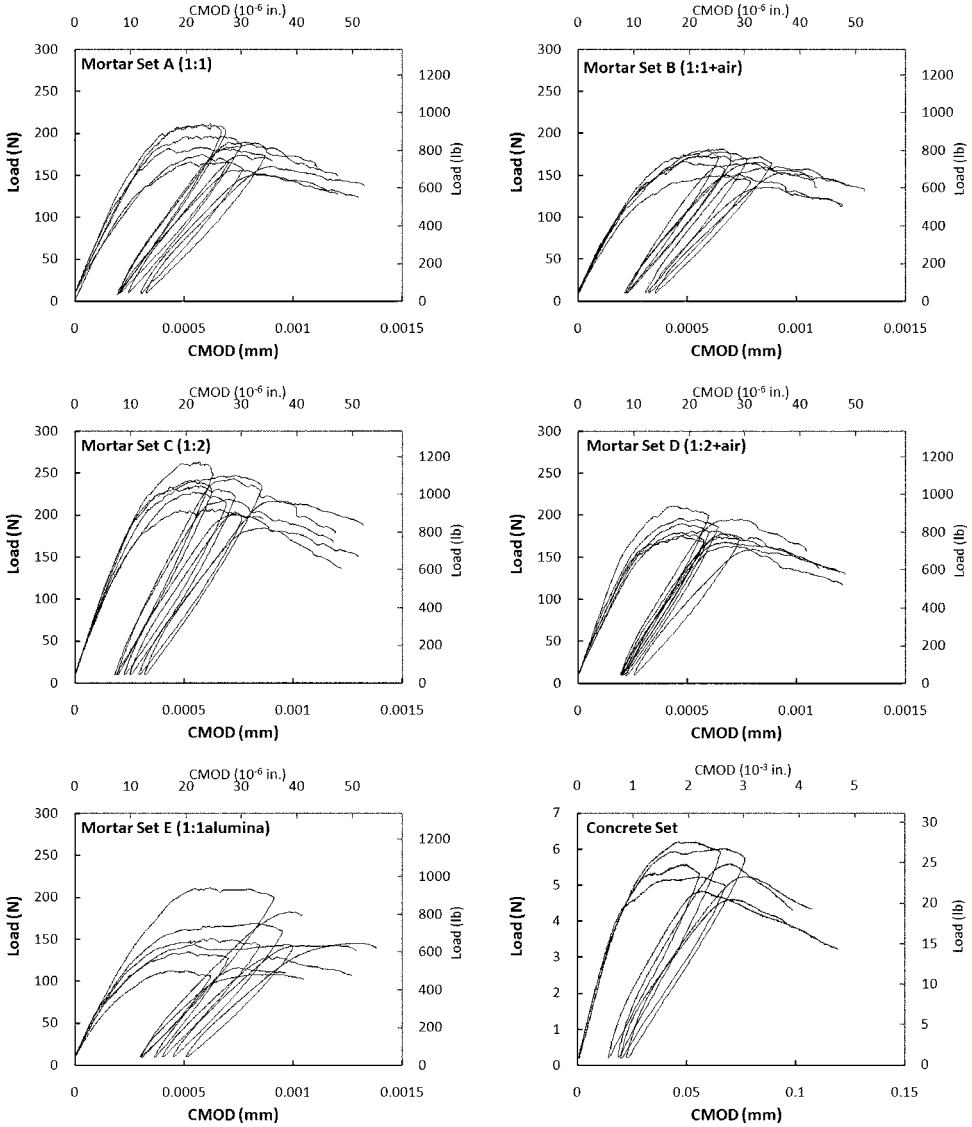

Fig. 1—Two-parameter fracture model testing for mortar and concrete beams.

Table 4—Average fracture parameters

Specimen set	Mortar A	Mortar B	Mortar C	Mortar D	Mortar E	Concrete
Young's modulus, GPa (10^3 ksi)	53.72 (7.8)	48.33 (7.0)	63.94 (9.3)	53.26 (7.7)	45.56 (6.6)	34.89 (5.1)
Modulus of rupture, MPa (ksi)	3.53 (0.51)	3.03 (0.44)	3.72 (0.54)	2.98 (0.43)	2.53 (0.37)	4.84 (0.70)
Critical crack length, mm (in.)	15.74 (0.62)	15.79 (0.62)	16.26 (0.64)	15.68 (0.62)	16.38 (0.64)	72.54 (2.86)
Critical K_{Ic}^s, $N/m^{1.5}$ (kips/in.$^{1.5}$)	405×10^3 (0.37)	350×10^3 (0.32)	451×10^3 (0.41)	345×10^3 (0.31)	310×10^3 (0.28)	1387×10^3 (1.26)
Critical $CTOD_c$, mm (10^{-3} in.)	1.45×10^{-3} (0.057)	1.41×10^{-3} (0.056)	1.48×10^{-3} (0.058)	1.22×10^{-3} (0.048)	1.48×10^{-3} (0.058)	21.95×10^{-3} (0.864)

stress intensity factor for the concrete set (geometrically proportional to the mortars by approximately a factor of 4) was over three times greater than the values measured for the mortars. The larger value is characteristic of the smaller effective length of the fracture process zone with respect to depth. In addition, the concrete contained large aggregate and a larger sand gradation than the mortars, influencing the heterogeneity of the microstructure.

Surface and crack imaging

The fracture surfaces were digitally imaged with a microscopy technique that recorded the surface topography and a surface image. In addition, three-dimensional (3-D) stereo image pairs were obtained of the fracture surfaces, which replicate depth as perceived from a single reference point. The cracks of the intact fracture specimens were intruded under pressure with a low-melting-point alloy, and digital images of the crack profiles were obtained. These techniques are described in the following section.

A laser-scanning confocal microscope was used to obtain images of the mortar surfaces.[12] The microscope uses a reflected laser light to measure the surface height by recording the in-focus plane from a series of vertical focal planes (or the z level) to produce a digital image of the z levels on an x-y grid, with high features appearing bright and low features appearing dark. An optical surface image was also captured at a magnification of 50×. By using a fluorescent filter, surface images of the reflective, dyed paste (bright) and nonreflective aggregate (dark) on the surface were obtained. Sixteen images, one from each sector in a 4 x 4 grid on the surface, were collected for each of the four samples in a mortar set.

To obtain the concrete surface topography, which exceeded the z-range capacity of the confocal microscope, 3-D stereo image pairs were used to calculate surface topography from the shift of the images relative to one another in conjunction with the rotation of the surface orientation between images. Three-dimensional stereo image pairs of the mortar surface at the same magnification as the confocal images were obtained using SEM by tilting the stage angle at a constant focal length. A charge-couple device (CCD) video camera was used to obtain image pairs of the concrete surfaces at a magnification of 4×. Five images were collected for each of the four samples in a material set: one from the center and four near each corner of the surface.

To characterize the crack profiles, the mortar specimens were cut to obtain the central portion of the beam containing the notch, which then was sectioned at the center of the beam width and close to each edge surface. The oven-dried sections were placed in an autoclave with pieces of solid Wood's metal, which is an alloy comprising bismuth, lead, tin, and cadmium with a low melting point near 66°C (151°F) and no appreciable volume change on solidification. The evacuated autoclave chamber was heated to above 90°C (194°F), pressurized to 10.3 MPa (1500 psi) for intrusion of the molten metal into the cracks, and allowed to cool to room temperature. The samples were prepared for imaging with backscatter electron microscopy (BSE). The high atomic weight of the Wood's metal alloy, compared to the mortar materials, provided sharp contrast in backscatter mode (bright).[12] Any unfilled cracks also appeared with high contrast (black).

Image analysis

The fracture surface images obtained by confocal microscopy, SEM, and digital video capture were analyzed to identify the location of intact aggregates, broken aggregates, aggregate impressions, and voids. To quantify crack branching from the profile micrographs, image analysis was performed to identify a main crack and measure the crack lengths of all branches.

An edge detection algorithm was used on the confocal images of the z-levels of the mortars to identify aggregate impressions and voids. A contrast enhancement algorithm was used on the fluorescent surface images to identify aggregates and paste.[12] Binary images of the location of these features were created, and they were assembled with the z-surface image into an image stack.

The 3-D stereo image pairs were analyzed by a commercial software program that determined the x, y, and z grid values for an array on the surface. The grid size for the mortar images was chosen to correspond to the pixel size of the confocal images, while the grid size for the concrete images matched the resolution with respect to the image size that was used for the mortar images.

For the 3-D stereo image pairs, the areas of intact aggregates, broken aggregates, aggregate impressions, and voids were identified visually from the perceived depth and topography and with a series of edge detection and area enclosure procedures.[12] The mortar images had no broken silica sand aggregate. An example binary stack for concrete is presented in Fig. 2, showing the surface image for reference.

The area fractions determined from the binary images and the roughness numbers are presented in Table 5. Higher area fractions of impressions and voids were identified for the 3-D stereo data, whereas slightly larger area fractions were identified for intact aggregate for the confocal data. Previous

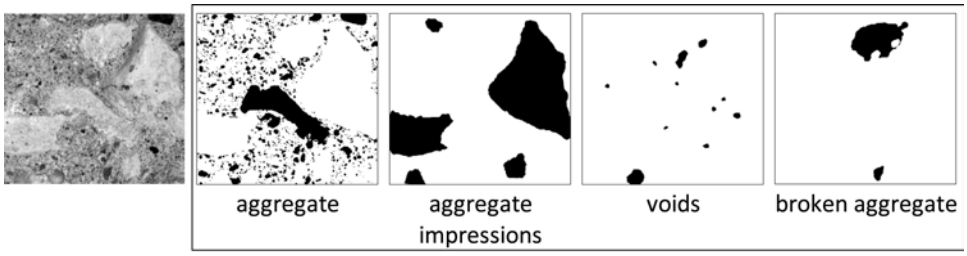

Fig. 2—Sample surface image and stack for 3-D stereo imaging of concrete.

Table 5—Average surface properties determined with image analysis

Material \ Image	Area, % Intact aggregates	Impressions	Voids	Broken aggregates	Roughness number
Confocal					
Mortar A	20.03	11.11	0.60	—	1.63
Mortar B	17.49	10.07	2.02	—	1.66
Mortar C	25.31	16.59	1.84	—	1.73
Mortar D	24.46	16.61	6.18	—	1.72
Mortar E	14.10	9.75	0.87	—	1.76
3-D stereo					
Mortar A	17.53	17.77	2.19	—	1.18
Mortar B	11.88	18.42	3.52	—	1.15
Mortar C	22.93	24.49	0.89	—	1.21
Mortar D	20.41	18.47	8.57	—	1.22
Mortar E	13.96	15.58	0.61	—	1.14
Concrete	25.60	13.65	1.19	18.04	1.19

work[12] comparing the mixture volumes of paste, sand, and air to the area fractions shows that the surfaces revealed higher paste volume, lower sand volume, and comparable air volume.The roughness number, which is the ratio of the total surface area as determined from triangulation between adjacent elevations to the total planar area, was higher for the confocal data, which indicates that more detail of the surface height is recorded than with the 3-D stereo technique.

The composite micrographs of the profiles of the central and near-edge cracks for the mortars were analyzed to identify the main crack profile and branches, as detailed in a previous paper.[12] Image analysis was used to identify the area of the crack intruded with Wood's metal and the area of the cracks, which were not intruded. A skeletonizing function was used to reduce the crack widths to single-pixel-wide lines, and the continuous crack path was identified and measured using orthogonal pixel neighbors and diagonal pixel neighbors. There was no identifiable difference in the crack formation of the midwidth section to that of the near-edge sections.

MICROMECHANICAL MODELING

The fracture energy determined by testing and the geometry, phases, and crack branching relationships obtained from microscopy and image analysis were the input data to a micromechanical model, and the results were used to investigate the contribution to toughness from mechanisms of crack deflection and branching with respect to the surface morphology. The model is able to characterize the fracture toughness of a theoretically flat crack devoid of toughening mechanisms by examining the local strain energy release rate.

Modeling of toughness

To evaluate the deflection-induced reduction in crack driving force, the strain energy release rate $\mathcal{G}$ of a crack that is deflected and twisted out of the plane of propagation for a matrix with inclusions based on Mode I (opening), Mode II (sliding), and Mode III (tearing) contributions has been determined by Faber and Evans[13] for tilting

$$\mathcal{G} = \frac{k_1^{t^2}\left(1-\nu^2\right)+k_2^{t^2}\left(1-\nu^2\right)}{E} \tag{1}$$

and twisting

$$\mathcal{G} = \frac{k_1^{T2}\left(1-\nu^2\right)+k_3^{T2}\left(1+\nu\right)}{E} \tag{2}$$

where $k_1{}^t$ and $k_2{}^t$ are the local stress intensity factors based on the angle of tilting and the Mode I stress intensity factor K_I; $k_1{}^T$ and $k_3{}^T$ are the local stress intensity factors based on the angles of tilt and twist with respect to $k_1{}^t$ and $k_2{}^t$ (refer to the Appendix);[14] ν is Poisson's ratio; and E is the modulus of elasticity.

The average strain energy release rate for the crack surface $\langle\mathcal{G}\rangle$ can be determined from Eq. (1) and (2) for the angle geometry and phase of every segment of a surface, while the strain energy release rate from plain strain, $\mathcal{G}_{flat}$, is related to the Mode I (opening) stress intensity factor for a flat crack where E_c is the elastic modulus for the cement paste

$$E_c\mathcal{G}_{flat} = K_I^2\left(1-\nu^2\right) \tag{3}$$

A toughening ratio for the stress intensity factor K_I can be defined in terms of the proportion of the strain energy release rate from plane strain to the reduced strain energy release rate for the surface using

$$\text{toughening ratio}_{\mathcal{G}} = \sqrt{\frac{\mathcal{G}_{flat}}{\langle\mathcal{G}\rangle}} = \sqrt{\frac{K_I^2\left(1-\nu^2\right)}{E_c\langle\mathcal{G}\rangle}} \tag{4}$$

To include the contribution of subsurface cracking, which is not accounted for in the average strain energy release rate, the effective toughening ratio can be determined by factoring the toughening ratio based on the strain energy

Table 6—Phase segment classification schema

Start phase	End phase	Segment classification
Void	Paste	Paste
Void	Aggregate	Interfacial paste
Void	Aggregate hole	Interfacial paste
Aggregate hole	Paste	Interfacial paste
Aggregate hole	Aggregate	Interfacial paste
Aggregate	Paste	Interfacial paste

release rate by the branching ratio function determined by crack micrograph analysis

$$\text{Toughening ratio} = \text{toughening ratio}_G \times \text{branching ratio} \quad (5)$$

The measured branching ratio values had a positive correlation with aggregate volume and with measured fracture toughness (Fig. 3) with no correlation with air void content. This suggests that the subsurface cracking mechanisms include aggregate interlock and interfacial transition zone fracture.

The image stacks containing the elevation data and the phase binaries were used to determine the angle of tilting and twisting and phase of each segment. When the ends of the segment were not of the same phase, the segment was classified as outlined in Table 6. Any segment at an aggregate boundary was considered to be interfacial paste. The phase identification was necessary to assign the elastic modulus to the segment in the local strain energy release rate calculation (Eq. (1) and (2)).

The model determines a toughening ratio that can quantify the toughness for a theoretical flat crack, K_m, with respect to the measured toughness

$$K_m = \frac{K_{Ic}^S}{\text{toughening ratio}} \quad (6)$$

where K_{Ic}^S is the critical stress intensity factor determined with the TPFM method.

Analysis of mechanisms

The model variables consisted of the elastic moduli of the phases, the Poisson's ratio, and the branching ratio function. In addition, the method of modeling the void segments could be specified. The void segment could be assigned an elastic modulus and behave as a "soft particle," with no increase in the strain energy release rate based on twisting or tilt. Alternatively, the void segment could contribute to the average strain energy release rate using the theoretical strain energy release rate for a flat, penny-shaped crack. This option required that the maximum failure stress derived from the flexure theory from maximum load during testing be specified.

Representative values of the elastic modulus were assigned for the cement paste, silica sand, crushed limestone, and ceramic alumina as 30.1 GPa (4.36×10^3 ksi), 70 GPa (10.1×10^3 ksi), 30.7 GPa (4.45×10^3 ksi), and 400 GPa (58.0×10^3 ksi), respectively.[15-17] The Poisson's ratio for all materials was 0.2. The elastic modulus of the interfacial paste was specified as a percentage of the elastic modulus of the cement paste based on an interfacial zone damage model.[15] A conservative damage of 15% was the equivalent of an elastic modulus

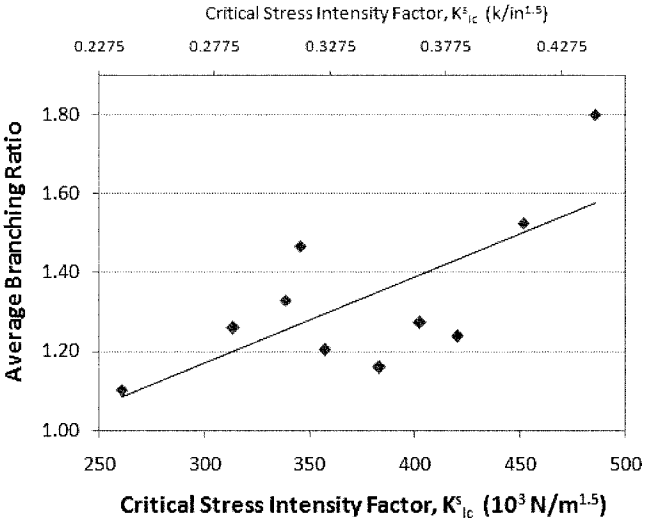

Fig. 3—Relationship of measured branching ratio to toughness.

of 85%. Lower values of 80, 75, and 70% were also investigated. When voids were modeled with elastic properties, the modulus was also specified as a percentage of the elastic modulus of the cement paste. Values of 50, 20, and 10% were investigated based on the interfacial zone damage model results[15] for fractional values of 1/2, 1/5, and 1/10 of the elastic modulus of the paste.

The branching ratio was assigned based on the critical stress intensity factor for the specimen and the linear regression fit of the average measured branching ratio to the critical stress intensity factor for the profiled specimens, as shown in Fig. 3. Because the subsurface crack profiles were not collected for the concrete specimens, the branching relationship for mortar was used for the concrete.

The modeling investigated the individual and combined effect of the material properties and branching. There were four conditions considered: 1) all surface (including voids) as homogeneous without crack branching to model deflection contribution; 2) all surface as paste to model void and crack branching contribution; 3) surface as aggregates and paste (no voids) to model stiffness contribution; and 4) surface as paste, aggregates, interfacial paste, and voids to model interfacial stiffness contribution. Figure 4 shows an example of the modeling results for the toughening ratio K_{Ic}^S/K_m for a mortar set (1:2 + air). Modeling all the surface as paste showed the largest increase from theoretical flat toughness K_m to measured toughness and would account for a toughness increase resulting only from surface tortuousity and branching. Modeling of the surface as aggregate behaving as inclusions in the paste was lower, but similar, as a result of interfacial paste at the aggregate boundaries, whereas the modeling that inluded the interfacial paste and modeled voids as penny-shaped cracks resulted in lower toughening ratios that were still significantly higher than the model results based on surface geometry.

For each set of image surface topography, binary phase data, and critical stress intensity factor K_{Ic}^S, the parametric study examined each of the four paste interface modulus variations with each of the four variations for void behavior (theoretical isolated penny-shaped cracks or soft interface) for a total of 16 modeled cases.

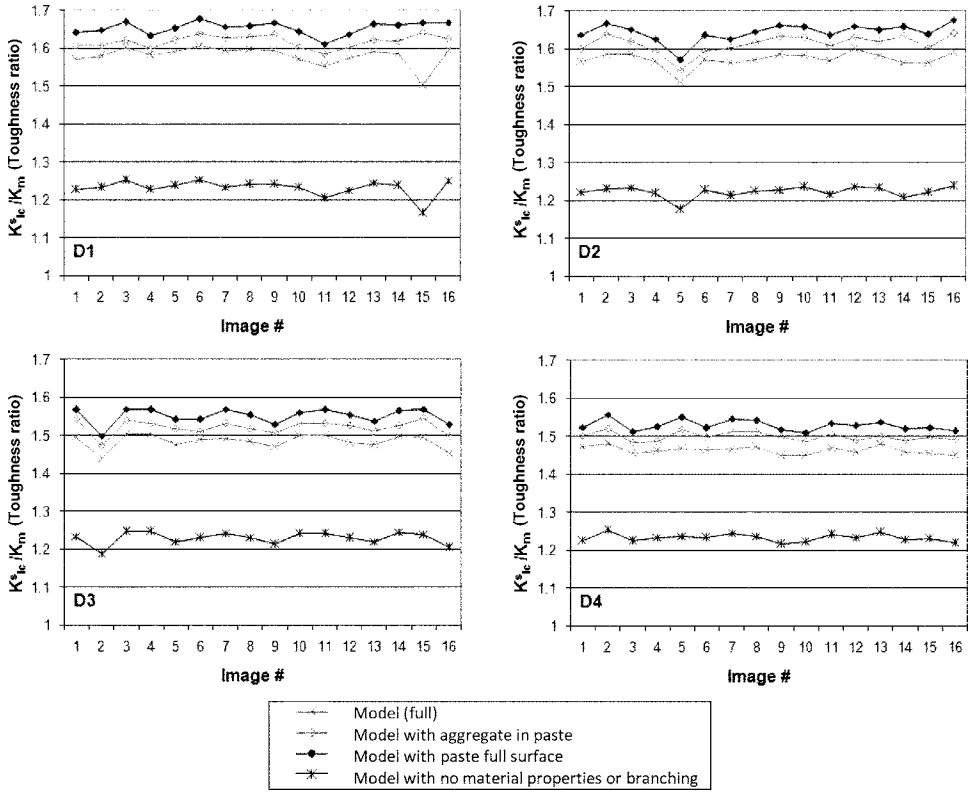

Fig. 4—Toughness ratio with model materials variation.

RESULTS

Void modeling

The modeling of voids as theoretical penny-shaped cracks based on the maximum tensile bending stress, which was a conservative estimate, resulted in little contribution to the toughening ratio, but had a similar effect as when voids were modeled as interfacial transition zone paste with a damage effect of 50%. As the "softness" of the void particles decreases, the influence of void content is considerable, resulting in toughness ratios of 1 or less. Figure 5 illustrates an example of the modeled toughness ratio for the sample set of Fig. 4.

The modeling of voids as theoretical penny-shaped cracks could not account for the influence on the strain energy release rate by multiple cracks (other voids) in close proximity to the void on the fracture surface. The surrounding voids may have had a similar strain energy release rate if the sizes were similar to the one on the surface—presumed to have reached the critical size to propagate—adding energy to the toughness. The voids in the path of the crack branches were accounted for only in the length of the branching and not by a direct contribution to the strain energy release rate. The air-entrained mortars with higher void content had lower toughening ratios, but also had lower measured fracture toughness.

The resulting flat crack toughness K_m for the analysis of voids as soft particles tended toward a mean value across all mortar sets of 250×10^3 N/m$^{1.5}$ (0.23 kips/in.$^{1.5}$) for the confocal data (Fig. 6) and 300×10^3 N/m$^{1.5}$ (0.27 kips/in.$^{1.5}$) for the 3-D stereo data (Fig. 7), with the exception of the control set containing the smooth ceramic aggregate. There was wider variation in the model results within the air-entrained sets and the ceramic aggregate set. The relatively lower measured fracture toughness for the control set was influenced by the accuracy of placement of the mixture within the central notched area, as the crack tended to propagate into the nearby plain paste.

The resulting flat crack toughness K_m for the analysis of voids as soft particles tended toward a mean value for the concrete of 400×10^3 N/m$^{1.5}$ (0.36 kips/in.$^{1.5}$) for the 3-D stereo data (Fig. 7). The concrete data had a higher quantity of voids, which led to a greater decrease in the toughening ratio than the mortars.

The parametric study of the mortar data indicates that there is a value between 20 and 50% of the paste modulus for the void for flat crack toughness. This estimation is similar to the values found by Yang[18] for the interfacial transition zone modulus over a 40 µm (0.0016 in.) width. There did not appear to be any indication of a trend for the damage effect with the limited sample population.

Interfacial paste modeling

The modeling of the interfacial paste modulus with a damage parameter indicated that 25 to 50% of the crack surface for the mortars and concrete was classified as interface. The amount is underestimated for the mortars because the image analysis did not quantify the interfacial transition zone thickness, but only recognized the interface as the distance between pixels (13.8 µm [0.0005 in.]) representing an aggregate boundary. The pixel distance for the concrete was somewhat larger than the measured interfacial zone thickness range of 50 to 100 µm at 138 µm (0.002 to 0.004 in. at 0.005 in.). Aggregate impressions were also considered as interfacial paste.

The parametric study of the damage parameter as represented by reducing the elastic modulus for the interfacial paste indicates that for the confocal data, a modulus of 70% of the paste modulus converges for a flat crack toughness, whereas a modulus of 75% converges for a flat crack toughness with the 3-D stereo data. The higher value for the 3-D stereo data appears to be directly related to the interface proportion determined by

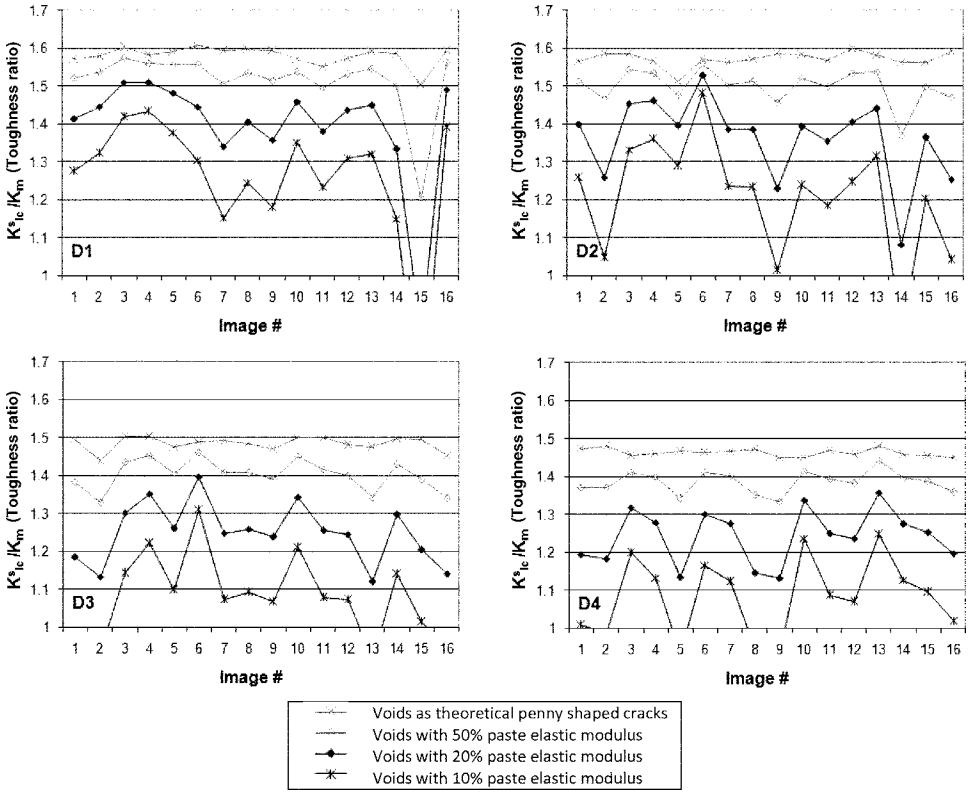

Fig. 5—Toughness ratio with model void variation.

the model for the images, as the values were on average 4% higher than the confocal data. Decreasing the interfacial paste modulus resulted in higher flat crack toughness, effectively contributing less to the toughening mechanisms. The interfacial transition zone is the preferential phase for crack development, and the phases of the segments on the fracture surface identified by the model indicate that the interfacial paste fraction was approximately half the size of the bulk paste matrix fraction for the mortars and approximately the same fraction as the bulk paste matrix for the concrete.

There was no indication of a convergent damage parameter for the flat crack toughness of the concrete with the limited sample population. If there was partial bond of the paste to the aggregate, as suggested by Hirsch,[19] the contribution of the interface paste to the toughness for the concrete would be overestimated. The parameters determined from the confocal and 3-D stereo data of the mortars for void modulus and interfacial zone modulus were used for the concrete modeling, as shown in Fig. 7.

The 3-D stereo image pairs had significantly less phase variation at a horizontal scale of 0.138 mm/segment (0.005 in./segment) for the concrete than a scale of 0.0138 mm/segment (0.0005 in./segment) for the mortars. If the scaling relationship could be quantified for the surface data, and for the surface topography, the flat crack toughness would be lower and would approach a unified value for the mortar materials composed of the same paste matrix.

Branching modeling

The modeling of the crack branching as a multiplier to the toughening ratio determined from the micromechanical model based on materials and surface tortuousity assumed that there was a constant proportion of energy used in the subsurface cracking from the mechanisms of branch formation, crack bridging, and aggregate interlock to the energy used to create the main crack surface. Because the branching ratio is based on the length of subsurface cracking in a planar section, it cannot directly quantify the energy in crack bridging and aggregate interlock and is a conservative measure. The branching ratios determined for the mortars without air entrainment and different sand volume were similar at averages of 1.41 (1:1) and 1.48 (1:2) and were also similar for the mortars with air entrainment and different sand volume at averages of 1.28 (1:1 + air) and 1.29 (1:2 + air). The average branching ratio for the control set was 1.16 (1:1alumina).

The branching ratio appears to be strongly influenced by the crack-arresting behavior of air voids off the main path. The section micrographs reveal the interconnectivity of the pore system along the length of the crack. In the air-entrained mortars, the percolation was greatest at the notch tip and decreased as the crack extended. In the mortar with the alumina balls, however, the percolation was uniform over the length of the crack. The porosity of the bulk paste was not treated differently for this material, although it most likely has a lower elastic modulus.

The average branching ratio modeled for the concrete, based on the relation of branching to measured toughness of the mortars, was 3.56. This is a 2.5-fold increase in the contribution of crack branching to the overall toughness of the concrete as that found for the mortar. The branching effect was anticipated to be larger because of the variation of the aggregate, the size of the fracture process zone, and the amount of microcracking expected from Mode II (shear) fracture[20] in addition to that from Mode I (opening). There was aggregate that had fractured in the concrete, which was rare in the mortar materials, and the contribution to the toughness was accounted for in the strain energy release rate based on the crack tilt and twist and the high elastic modulus

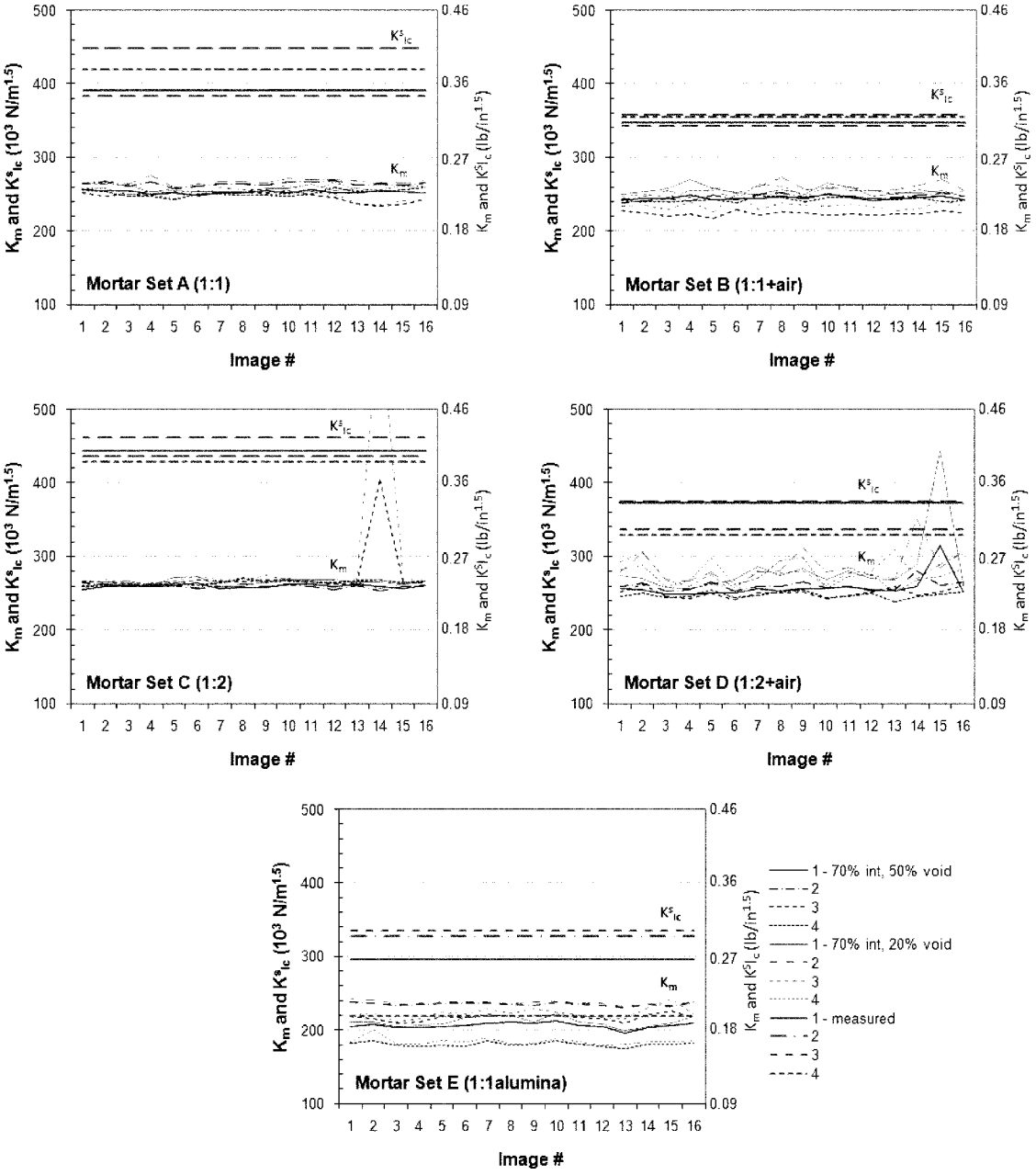

Fig. 6—Modeled flat crack fracture toughness for mortars by confocal data.

of the aggregate. If the crack branches were arrested by the aggregate fissures or contributed to their fracture, the branching ratio modeled was unable to account for it.

Surface geometry technique

The surface geometry measurement technique was not a parametric variable in the modeling, but it did influence the results. The finer level of detail measured by confocal microscopy resulted in higher toughening ratios and lower flat crack toughness than the 3-D stereo technique. The variation of the toughening ratio of the 3-D stereo data to the toughening ratio of confocal mortar data was almost consistently between 9 and 11% for all sand mortars, and nearly 18% for the alumina ball mortar. The confocal surface data were filtered for noise resulting from the reflective silica aggregate under the focused laser beam and the absence of light reflection at the aggregate boundaries with the paste.[5] The 3-D stereo technique resulted in smoother, noise-free surfaces at the same horizontal grid (*xy*) scale as the confocal measurement, but with a slightly smaller vertical (*z*) scale. Figure 8(a) and (b) illustrates the surface variation of mortar by technique at the same scale. The surface detail for the concrete images was lower as well, and is shown at a reduced scale in Fig. 8(c).

SUMMARY AND CONCLUSIONS

This study successfully established a quantitative link between fracture surface parameters and mechanical test results for a variety of quasi-brittle cement-based materials. The modeling of mortar and concrete toughness through a parametric study allowed the investigation of material and mechanical properties of fracture in cement-based materials. The modeling of voids, interfacial paste modulus, and branching ratio were evaluated with respect to their contribution to toughness in relation to a theoretical flat crack toughness devoid of toughening mechanisms.

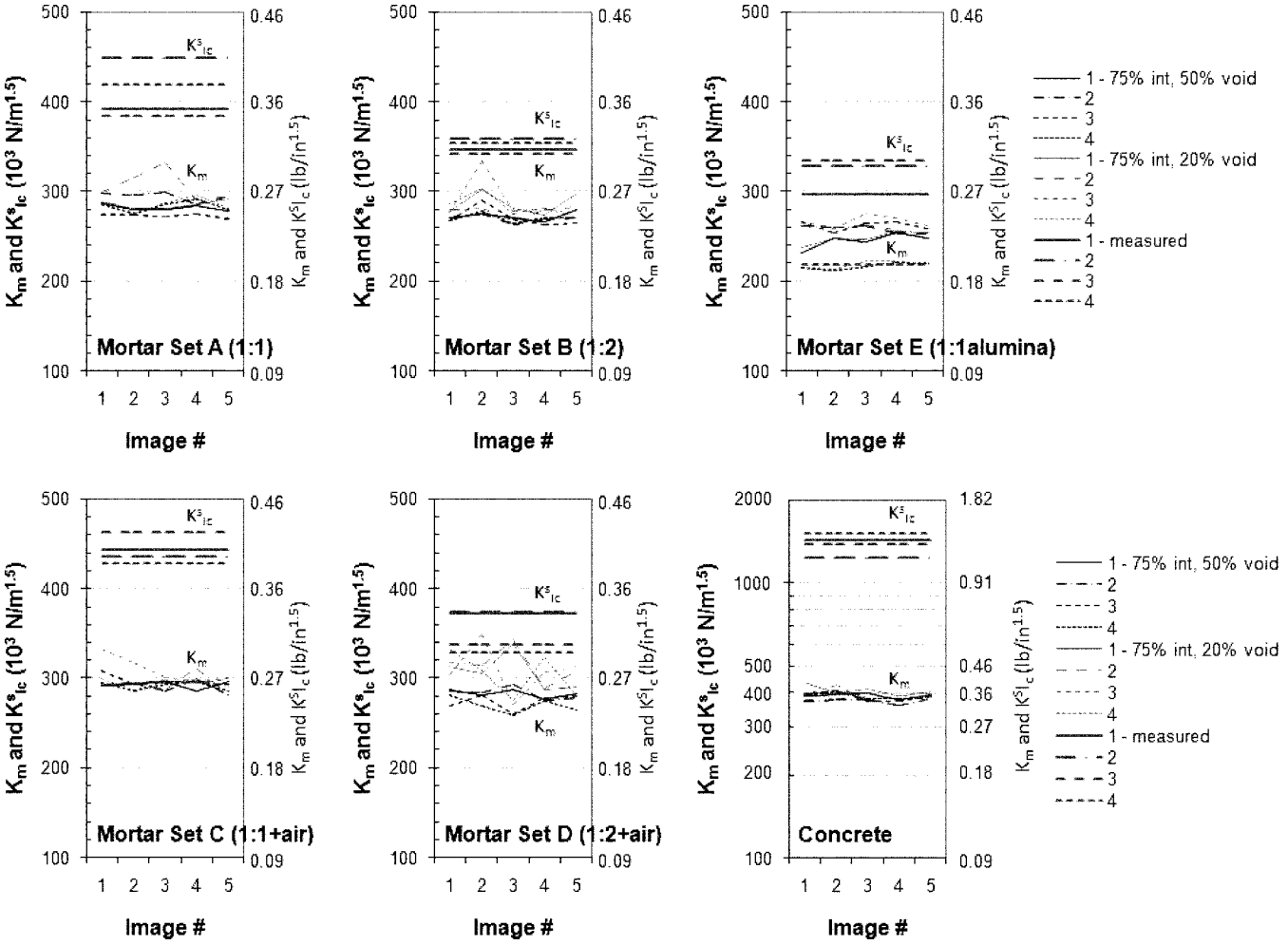

Fig. 7—Modeled flat crack fracture toughness for mortars and concrete by 3-D stereo data.

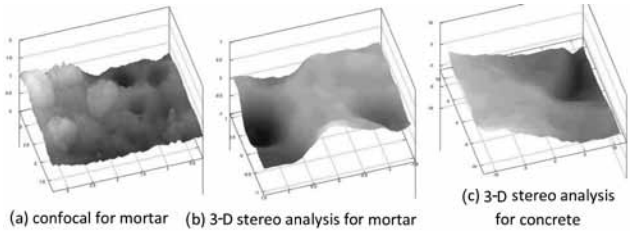

Fig. 8—Topographic detail by material and surface technique (identical scale for mortars only).

The results indicate that the effect of phases, modulus of elasticity, air voids, and branching mechanisms on the toughening was significant. The treatment of void segments as soft particles, rather than penny-shaped cracks, modeled the material behavior better, although a method to include the shielding effect of the subsurface voids based on the spatial void distribution from stereology and the influence of shrinkage cracks may prove insightful. The void modulus had more influence on the toughening ratio than the interfacial paste modulus.

The effect of reducing the value of the modulus of elasticity for the interfacial paste resulted in an expected increase in theoretical flat crack toughness. The interfacial transition zone has been identified as the preferential phase for crack development, and the surface phases identified by the model quantified the interface fraction as approximately half the size of the paste matrix fraction for the mortars and the interface fraction as slightly larger than the paste matrix fraction for the concrete. The model results for the concrete indicate that changes to the interface modulus do not significantly impact the theoretical flat crack toughness, which may suggest that the modeling of the interfacial paste through a damage function was an oversimplification. The type of aggregate may affect the porosity of the interfacial paste as well.

The branching modeling for the concrete, based on the evidence in the mortars, supports the assumption of significant microcrack formation under Mode I loading. There was no measurable evidence of aggregate interlock that would hinder the crack opening. This mechanism may have contributed more to the toughness of the concrete material than the mortars.

The modeling of the strain energy release rate as a function of the crack segment geometry determined from topographical imaging and material identification from image analysis was based on the assumption that the materials behaved linear-elastically at the microstructural level, whereas the toughening mechanisms contributed to the nonlinear elastic macrostructural behavior. The modeling attempted to quantify the contribution to toughness measured with mechanical testing, thereby defining a theoretical flat

crack toughness determined to be 250×10^3 N/m$^{1.5}$ (0.23 kips/in.$^{1.5}$) for the confocal microscopy mortar data, 300×10^3 N/m$^{1.5}$ (0.27 kips/in.$^{1.5}$) for the 3-D stereo mortar data, and 400×10^3 N/m$^{1.5}$ (0.36 kips/in.$^{1.5}$) for the 3-D stereo concrete data.

The analysis indicated a correlation to the experimental results when void segments were modeled as soft particles with a modulus of 20 to 50% of the cement paste and an interfacial paste modulus of 70 to 75% of the cement paste.

Without techniques to precisely measure the microstructural behavior, modeling provides a basis of comparison to the observed behavior for a greater understanding of quasi-brittle mortar and concrete materials. The model results indicate that there is a convergence toward a single value of toughness for cement materials with the same paste matrix by quantifying the additional energy required by crack deflection, crack branching and aggregate interlock, and phase mechanics.

ACKNOWLEDGMENTS

This research was supported by the NSF Center for Advanced Cement-Based Materials (NSF Grant No. DMR 88808432-01).

NOTATION

AC = absorption capacity
CMOD = crack mouth opening displacement
$CTOD_c$ = critical crack tip opening displacement
E = modulus of elasticity
E_c = modulus of elasticity for cement paste
FM = fineness modulus
$\mathcal{G}$ = strain energy release rate of deflected or tilted crack segment
$\mathcal{G}_{flat}$ = strain energy release rate of flat crack
$\langle \mathcal{G} \rangle$ = average strain energy release rate
K_I = flat crack stress intensity factor for Mode I (opening)
K_{IC} = critical stress intensity factor for Mode I (opening)
K_{Ic}^S = critical stress intensity factor (two-parameter model method)
k_1^t = local stress intensity factor for tilted crack strain energy release rate
k_2^t = local stress intensity factor for tilted crack strain energy release rate
k_1^T = local stress intensity factor for twisted crack strain energy release rate
k_3^T = local stress intensity factor for twisted crack strain energy release rate
TM = total moisture
γ_{SSD} = bulk specific gravity, saturated surface-dry
ν = Poisson's ratio

REFERENCES

1. Hillerborg, A., "The Theoretical Basis of a Method to Determine the Fracture Energy G_F of Concrete," *Materials and Structures*, V. 18, No. 106, 1985, pp. 291-296.

2. Shah, S. P.; Swartz, S. E.; and Ouyang, C., *Fracture Mechanics of Concrete*, John Wiley & Sons, New York, 1995, 552 pp.

3. Mindess, S., and Young, J. F., *Concrete*, Prentice-Hall, Englewood Cliffs, NJ, 1981.

4. Mindess, S., and Diamond, S., "The Cracking and Fracture of Mortar," *Materials and Structures*, V. 15, No. 86, 1982, pp. 107-113.

5. Abell, A. B., "Microstructure and Its Relationship to Fracture in Portland Cement Mortar and Concrete," PhD thesis, University of Illinois at Urbana-Champaign, Urbana, IL, 2000, 237 pp.

6. RILEM Draft Recommendations, TC89-FMT Fracture Mechanics of Concrete—Test Methods, "Determination of Fracture Parameters (K_{Ic}^S and $CTOD_c$) of Plain Concrete Using Three-Point Bend Tests," *Materials and Structures*, V. 23, 1990, pp. 457-460.

7. Jenq, Y. S., and Shah, S. P., "A Two Parameter Fracture Model for Concrete," *Journal of Engineering Mechanics*, V. 111, No. 4, 1985, pp. 1227-1241.

8. Abell, A. B., and Lange, D. A., "The Role of Crack Deflection in Toughening of Cement-Based Material," *International Symposium Proceedings*, Brittle Matrix Composites 5, A. M. Brant, V. C. Li, and I. H. Marshall, eds., BIGRAF and Woodhead Publishing, Warsaw, Poland, 1997, pp. 241-250.

9. Radjy, F., and Hansen, T. C., "Fracture of Hardened Cement Paste and Concrete," *Cement and Concrete Research*, V. 3, No. 4, 1973, pp. 343-361.

10. Moavenzadeh, F., and Kuguel, R., "Fracture of Concrete," *Journal of Materials*, V. 4, No. 3, 1969, pp. 497-519.

11. Ouyang, C., and Shah, S. P., "Geometry-Dependent *R*-Curve for Quasi-Brittle Materials," *Journal of the American Ceramic Society*, V. 74, No. 11, 1991, pp. 2831-2836.

12. Nichols, A. B., and Lange, D. A., "3D Surface Image Analysis for Fracture Modeling of Cement-Based Materials," *Cement and Concrete Research*, V. 36, No. 6, 2006, pp. 1098-1107.

13. Faber, K. T., and Evans, A. G., "Crack Deflection Processes—I. Theory," *Acta Metallurgica*, V. 31, No. 4, 1983, pp. 565-576.

14. Abell, A. B., and Lange, D. A., "Fracture Mechanics Modeling Using Images of Fracture Surfaces," *International Journal of Solids and Structures*, V. 35, No. 31-32, 1997, pp. 4025-4034.

15. Lutz, M. P.; Monteiro, P. J. M.; and Zimmerman, R. W., "Inhomogeneous Interfacial Transition Zone Model for the Bulk Modulus of Mortar," *Cement and Concrete Research*, V. 27, No. 7, 1997, pp. 1113-1122.

16. Lawn, B. R., *Fracture of Brittle Solids*, second edition, Cambridge University Press, Cambridge, MA, 1993, 55 pp.

17. Nilsen, A. U., and Monteiro, P. J. M., "Concrete: A Three Phase Material," *Cement and Concrete Research*, V. 23, No. 1, 1993, pp. 147-151.

18. Yang, C. C., "Effect of the Transition Zone on the Elastic Moduli of Mortar," *Cement and Concrete Research*, V. 28, No. 5, 1998, pp. 727-736.

19. Hirsch, T. J., "Modulus of Elasticity of Concrete Affected by Elastic Moduli of Cement Paste Matrix and Aggregate," ACI JOURNAL, *Proceedings* V. 59, No. 3, 1962, pp. 427-452.

20. Landis, E., and Shah, S. P., "The Influence of Microcracking on the Mechanical Behavior of Cement Based Materials," *Journal of Advanced Cement Based Materials*, V. 2, No. 3, 1995, pp. 105-118.

APPENDIX[13]

Tilted segment factors (θ):

$$k_1^t = \cos^3\left(\frac{\theta}{2}\right) K_I$$

$$k_2^t = \sin\left(\frac{\theta}{2}\right)\cos^2\left(\frac{\theta}{2}\right) K_I$$

Twisted segment factors (ϕ):

$$k_1^T = \cos^4\left(\frac{\theta}{2}\right)\left[2\nu\sin^2\phi + \cos^2\left(\frac{\theta}{2}\right)\cos^2\phi\right] k_1^t + \sin^2\left(\frac{\theta}{2}\right)\cos^2\left(\frac{\theta}{2}\right)\left[2\nu\sin^2\phi + 3\cos^2\left(\frac{\theta}{2}\right)\cos^2\phi\right] k_2^t$$

$$k_3^T = \cos^4\left(\frac{\theta}{2}\right)\left[\sin\phi\cos\phi\left(\cos^2\left(\frac{\theta}{2}\right) - 2\nu\right)\right] k_1^t + \sin^2\left(\frac{\theta}{2}\right)\cos^2\left(\frac{\theta}{2}\right)\left[\sin\phi\cos\phi\left(3\cos^2\left(\frac{\theta}{2}\right) - 2\nu\right)\right] k_2^t$$